Vortex shedding model of a flapping flag

SÉBASTIEN MICHELIN[1,2]†
STEFAN G. LLEWELLYN SMITH[1]
AND BEVERLEY J. GLOVER[3]

[1]Department of Mechanical and Aerospace Engineering, Jacobs School of Engineering,
UCSD, La Jolla CA 92093-0411, USA

[2]Ecole Nationale Supérieure des Mines de Paris, 60–62 Boulevard Saint Michel,
75272 Paris cedex 06, France

[3]Departement of Plant Sciences, University of Cambridge, Downing Street,
Cambridge CB2 3EA, UK

A two-dimensional model for the flapping of an elastic flag under axial flow is described. The vortical wake is accounted for by the shedding of discrete point vortices with unsteady intensity, enforcing the regularity condition at the flag's trailing edge. The stability of the flat state of rest as well as the characteristics of the flapping modes in the periodic regime are compared successfully to existing linear stability and experimental results. An analysis of the flapping regime shows the co-existence of direct kinematic waves, travelling along the flag in the same direction as the imposed flow, and reverse dynamic waves, travelling along the flag upstream from the trailing edge.

1. Introduction

A fluttering instability can develop from the interaction of the internal dynamics of an elastic structure and an axial flow. The flapping of wind-forced flags is a canonical example of such an interaction problem, which is also of interest in various other engineering (Watanabe *et al.* 2002) and medical applications (Huang 1995; Balint & Lucey 2005). This instability arises from the competition between the destabilizing effect of the aerodynamic pressure and the stabilizing effect of the (small) bending rigidity of the structure.

The fluttering flag instability has been the focus of a large number of experimental studies including soap-film (Zhang *et al.* 2000), water-tunnel (Shelley, Vandenberghe & Zhang 2005) and wind-tunnel experiments (Eloy *et al.* 2008). Recently full numerical simulations of the coupled fluid and solid dynamics have been carried out using immersed-boundary methods (Zhu & Peskin 2002) and coupled fluid–solid solvers (Connell & Yue 2007). The latter study identified three possible behaviours for the flag: stable and flat, periodic flapping, and chaotic.

To understand the onset of the instability, several papers have focused on the linear stability of the flat position. The two-dimensional linear stability of infinite membranes under axial flow was first studied by Rayleigh (1878). More recently, Kornecki, Dowell & O'Brien (1976) carried out a linear stability study of the two-dimensional problem, modelling the wake behind a finite-length clamped plate as a distribution of vorticity (see Eloy *et al.* 2008, with increased numerical resolution).

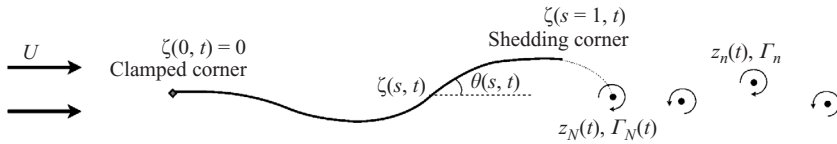† Email address for correspondence: smichelin@ucsd.edu

FIGURE 1. Vortex shedding behind a flapping flag. The oncoming flow is horizontal and vortices are shed from the trailing edge. The last vortex has unsteady intensity, the other vortices have frozen circulation.

Eloy, Souilliez & Schouveiler (2007) carried out a linear stability analysis including three-dimensional effects.

The purpose of the present work is to propose a reduced-order model for the flow over the flag, able to obtain the long-time behaviour and finite-amplitude flapping. It also reproduces the main characteristics of the problem as observed in full numerical simulations and experiments while significantly reducing the computational complexity. A potential flow representation is used for the two-dimensional flow past an infinitely thin inextensible elastic strip of finite length. The wake is represented by discrete point vortices, unlike the vortex sheet representation described in Alben & Shelley (2008). Here, the intensity of the last point vortex shed is adjusted in time to satisfy the regularity of the flow velocity at the trailing edge (Brown–Michael vortex) and a new vortex is shed when the previous one reaches a maximum intensity (Cortelezzi & Leonard 1993; Michelin & Llewellyn Smith 2008).

2. Model

A two-dimensional model of a flapping flag is considered. The flag is inextensible and clamped at its fixed end; L, B and ρ_s are respectively its length, bending rigidity and mass per unit length. The surrounding fluid density is ρ, and a uniform horizontal flow at infinity U_∞ is prescribed. In the following, all quantities are non-dimensionalized using L, U_∞ and ρ as reference values. Positions and velocities are defined with respect to a fixed system of axes with origin at the clamped end of the flag.

2.1. *Solid model*

A finite-displacement inextensible Euler–Bernoulli beam model is considered. The position of the flag is $\zeta(s,t)$ ($0 \leqslant s \leqslant 1$ is the arclength), and $\theta(s,t)$ is the angle between the local tangent and the horizontal axis (see figure 1). Using the Euler–Bernoulli assumption for a slender beam ($M = -\eta\theta_s$ with M the elastic torque along the flag and η the non-dimensional bending rigidity), and defining $T(s,t)$ to be the tension along the flag, Newton's second law and the inextensibility condition become

$$\mu\ddot{\zeta} = [e^{i\theta}(T - i\eta\theta_{ss})]_s - i[p]^{\pm}e^{i\theta}, \qquad \zeta_s = e^{i\theta} \tag{2.1}$$

where a subscript s stands for $\partial/\partial s$ and dotted variables for $\partial/\partial t$, with clamped-free boundary conditions:

$$\zeta(0,t) = \theta(0,t) = 0, \qquad \theta_s(1,t) = \theta_{ss}(1,t) = T(1,t) = 0. \tag{2.2}$$

This model is equivalent to the one used in Alben & Shelley (2008). Here $\mu = \rho_s/\rho L$ and $\eta = B/\rho U_\infty^2 L^3$ are respectively the non-dimensional flag density and bending rigidity, where $\sqrt{\eta}$ is also the time-scale ratio of the response to the pressure forcing and the bending stiffness. For comparison purposes with the linear stability results of Eloy *et al.* (2008) we will also use in the following the alternative non-dimensional

parameters

$$M^* = \frac{1}{\mu} = \frac{\rho L}{\rho_s}, \qquad U^* = \sqrt{\frac{\mu}{\eta}} = U_\infty L \sqrt{\frac{\rho_s}{B}}. \qquad (2.3)$$

U^* is the free-stream velocity non-dimensionalized by the flag rigidity and inertia.

2.2. *Vortex shedding model*

The flow around the flag is assumed to be irrotational. To satisfy the regularity condition for the flow at the trailing edge, point vortices are introduced following the method suggested by Cortelezzi & Leonard (1993) and Cortelezzi (1996) for the prescribed flow over fixed semi-infinite and finite plates, and applied in Michelin & Llewellyn Smith (2008) to the coupled motion of a falling card and the surrounding fluid. In this approach, one point vortex with unsteady intensity is released from each shedding corner. At each time step, the intensity is adjusted so as to satisfy the regularity condition: the flow velocity w must remain finite at the trailing edge. These vortices, with position z_n and intensity Γ_n, are also known as Brown–Michael point vortices (Brown & Michael 1954; Rott 1956), and obey the modified equation of motion

$$\dot{z}_n + (z_n - z_{n,0})\frac{\dot{\Gamma}_n}{\Gamma_n} = \overline{\tilde{w}_n}, \qquad (2.4)$$

where the overbar denotes the complex conjugate. The second term accounts for the conservation of fluid momentum around the vortex and associated branch cut, and $\tilde{w}_n$ is the desingularized flow velocity at the vortex position (Saffman 1992).

When a vortex reaches maximum intensity, the intensity of this vortex is frozen and a new vortex is started from the shedding corner. Because the angle of attack is always small in this problem, vortex shedding is neglected at the leading edge and vortices are shed from the trailing edge only. Therefore at any time, the vortex wake consists of $N - 1$ vortices $(z_j(t), \Gamma_j)$ with steady intensity and one unsteady point vortex $(z_N(t), \Gamma_N(t))$.

2.3. *Fluid model*

The potential flow around the deformable flag can be solved by representing the infinitely thin flag as a bound vorticity distribution κ (Jones 2003; Shukla & Eldredge 2007; Alben & Shelley 2008). The complex fluid velocity is the superposition of a uniform flow at infinity, and the contribution of the vorticity distribution (bound vortex sheet for the flag and point vortices for the wake):

$$w = U_\infty + \frac{1}{2\pi i}\left[\int_0^1 \frac{\kappa\, \mathrm{d}s}{z - \zeta(s,t)} + \sum_{j=1}^N \frac{\Gamma_j}{z - z_j}\right].$$

Using the Plemelj formula and following Shukla & Eldredge (2007), the normal flow boundary condition on the flag $\mathrm{Im}[e^{-i\theta}(\bar{w} - \dot{\zeta})] = 0$ becomes a Fredholm singular integral equation for κ. Assuming the system is started from rest, the total circulation at infinity must vanish at all time (Kelvin's circulation theorem). Together with the regularity condition $w(\zeta(1,t),t) \neq \infty$, these two conditions can be rewritten as a system of equations for κ and the intensity Γ_N of the last shed vortex (the others are known and frozen):

$$\frac{1}{2\pi}\fint_0^1 \mathrm{Re}\left[\frac{e^{i\theta(s_0)}}{\zeta(s_0) - \zeta(s)}\right]\kappa\, \mathrm{d}s = \mathrm{Im}\left[e^{i\theta(s_0)}\left(U_\infty + \frac{1}{2\pi i}\sum_{j=1}^N \frac{\Gamma_j}{\zeta(s_0) - z_j} - \dot{\bar{\zeta}}\right)\right], \quad (2.5a)$$

$$\int_0^1 \kappa\, \mathrm{d}s + \sum_{j=1}^N \Gamma_j = 0, \qquad \kappa(1,t) = 0, \qquad (2.5b)$$

where the integral on the left-hand side of (2.5a) is understood as the principal value. Note that because of the Cauchy-like form of the kernel in (2.5a), the first condition in (2.5b) is necessary for the problem for κ to be well-posed.

The desingularized velocity $\tilde{w}_n$ in (2.4) is

$$\tilde{w}_n = U_\infty + \frac{1}{2\pi i} \left[\int_0^1 \frac{\kappa \, ds}{z_n - \zeta(s,t)} + \sum_{j \neq n} \frac{\Gamma_j}{z_n - z_j} \right]. \tag{2.6}$$

The initial position of the vortex at the corner of the solid induces a singularity in (2.6). A small-time expansion of the vortex position can be performed following Cortelezzi & Leonard (1993) and Michelin & Llewellyn Smith (2008) and the resulting analytic small-time solution is used for the first time step of each new vortex.

From Bernoulli's theorem, the pressure jump across the flag is

$$[p]^\pm(s_0) = \int_0^{s_0} \dot{\kappa} \, ds + \kappa(s_0) w_p(s_0), \tag{2.7}$$

with w_p the average of the relative tangential fluid velocities on either sides of the flag (Jones 2003; Alben & Shelley 2008)

$$w_p(s_0) = \text{Re} \left[e^{i\theta(s_0)} \left(\frac{1}{2\pi i} \fint_0^1 \frac{\kappa(s) \, ds}{\zeta(s_0) - \zeta(s)} + U_\infty - \sum_{j=1}^N \frac{i\Gamma_j}{2\pi(\zeta(s_0) - z_j)} - \dot{\bar{\zeta}}(s_0) \right) \right].$$

2.4. *Numerical method for the flag problem*

A system of equations for θ and T alone can be obtained by combining both equations in (2.1):

$$T_{ss} - \theta_s^2 T = -[p]^\pm \theta_s - 2\eta_s \theta_{sss} - \eta\theta_{ss}^2 - \mu_s \dot{\theta}^2, \tag{2.8a}$$

$$\mu_s \ddot{\theta} = -[p]_s^\pm - \eta\theta_{ssss} + (T + \eta\theta_s^2)\theta_{ss} + 2T_s\theta_s. \tag{2.8b}$$

Determining the flag position as $\zeta(s,t) = \int_0^s e^{i\theta} \, ds'$ automatically satisfies the inextensibility condition. Then the boundary conditions are obtained from (2.2) and Newton's second law applied to the whole flag as

$$\theta(0,t) = \theta_s(1,t) = \theta_{ss}(1,t) = T(1,t) = 0, \tag{2.9a}$$

$$\mu_s \int_0^1 \int_0^s e^{i\theta}(i\ddot{\theta} - \dot{\theta}^2) \, ds' \, ds = -T(0) + i\eta\theta_{ss}(0) - i \int_0^1 [p]^\pm e^{i\theta} \, ds. \tag{2.9b}$$

Expanding θ as a superposition of Chebyshev polynomials $\theta = \sum c_j(t) T_j(2s - 1)$, (2.4), (2.5), (2.7) and (2.8) are used to integrate c_j and (z_n, Γ_n) in time using a second-order-accurate finite-difference scheme. The fourth-order derivative in space in (2.8b) is treated semi-implicitely and all nonlinear terms in (2.8) are evaluated explicitly. Chebyshev spectral methods are particularly adapted to handle the square-root singular behaviour of the general solution of (2.5a) near $s = 0$ and $s = 1$. From (2.4), (2.6) and the time derivative of (2.5), $\dot{\Gamma}_N$, $\dot{z}_n$, $\dot{\kappa}$ and therefore $[p]^\pm$ depend on $\ddot{\theta}$ linearly. In (2.8), the contribution of the solid acceleration to the pressure (added inertia) can be isolated to compute $\ddot{c}_j$ directly, thereby greatly reducing the computational cost in comparison with other methods which require an iterative solver at each time-step of the fluid–solid problem (Alben & Shelley 2008). The second-order accuracy of the solver was checked using (2.1) and the conservation of
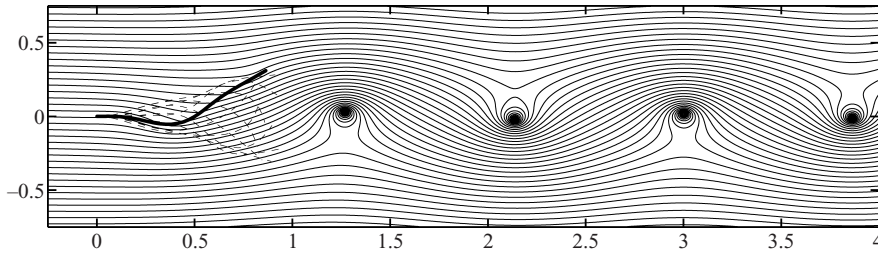
FIGURE 2. Instantaneous streamlines for the flow over the flapping flag in the periodic regime for $M^* = 3$ and $U^* = 11.5$. The grey lines are the streamlines. For reference, the successive positions of the flag in a flapping cycle are plotted as black dashed lines.

the flag energy:

$$\dot{E} = W_p, \quad \text{with } E = \int_0^1 \left[\frac{1}{2} \mu |\dot{\zeta}|^2 + \frac{1}{2} \eta \theta_s^2 \right] \mathrm{d}s, \quad W_p = -\int_0^1 [p]^{\pm} \mathrm{Im}[\dot{\zeta} \mathrm{e}^{-\mathrm{i}\theta}] \mathrm{d}s. \quad (2.10)$$

3. Results

The flag is initially at rest ($\theta(s, t < 0) = 0$) and at $t = 0$ the horizontal flow at infinity is ramped up continuously to its long-time value. A small transient vertical perturbation is added to perturb this trivial equilibrium (of the form $v = \epsilon t^p \mathrm{e}^{-qt}$; different values of p and q were tested with no significant impact on the long-time behaviour). In each run, the rigidity and inertia of the flag are fixed, and the flow at infinity can be varied inducing a change of the non-dimensional velocity U^* defined in (2.3).

3.1. *Three possible regimes*

For a given inertia ratio M^*, three regimes were observed. For small U^* (low wind speed), the initial perturbation creates a small motion of the flag that quickly decays, and the flag returns to its rest position.

When U^* is increased above a critical value U_c^* ($U_c^* = 9.6$ for $M^* = 3$), this rest position becomes unstable. For intermediate values of U^* ($9.6 \leqslant U^* \leqslant 12$ for $M^* = 3$), a periodic flapping develops after a transient regime, in which the energy of the flag oscillates with an exponentially growing envelope. One point vortex is shed during each half-stroke and the intensity of the point vortices have alternating signs. Downstream from the flag (about one flag length), these point vortices arrange in a weak von Kármán street and are advected with U_∞ close to the horizontal axis (figure 2). This is in good agreement with the positioning of the centres of vorticity in the vortex sheet approach (Alben & Shelley 2008). This situation differs significantly from thrust-generating flapping, where the vortices are advected faster due to their reversed von Kármán arrangement.

The motion of the flag in this flapping regime is highly periodic. The power spectra of the flag total energy (2.10) and tail orientation $\theta(1, t)$ display sharp peaks (see the left-hand column of figure 3a, b). Note that the orientation spectrum contains only odd harmonics ($\omega_0, 3\omega_0 \ldots$) while the energy is a quadratic function of the kinematic variables and its spectrum only contains the even harmonics ($2\omega_0, 4\omega_0, \ldots$). In the phase plot of the flag tail position, the outgrowing spiral corresponds to the instability development from the initial rest position, and convergence to a limit-cycle is clearly seen for $U^* \leqslant 12$ (centre column of figure 3). The decreasing number of oscillations (or spiral turns) shows an increase of the instability growth rate with $U^* - U_c^*$. The
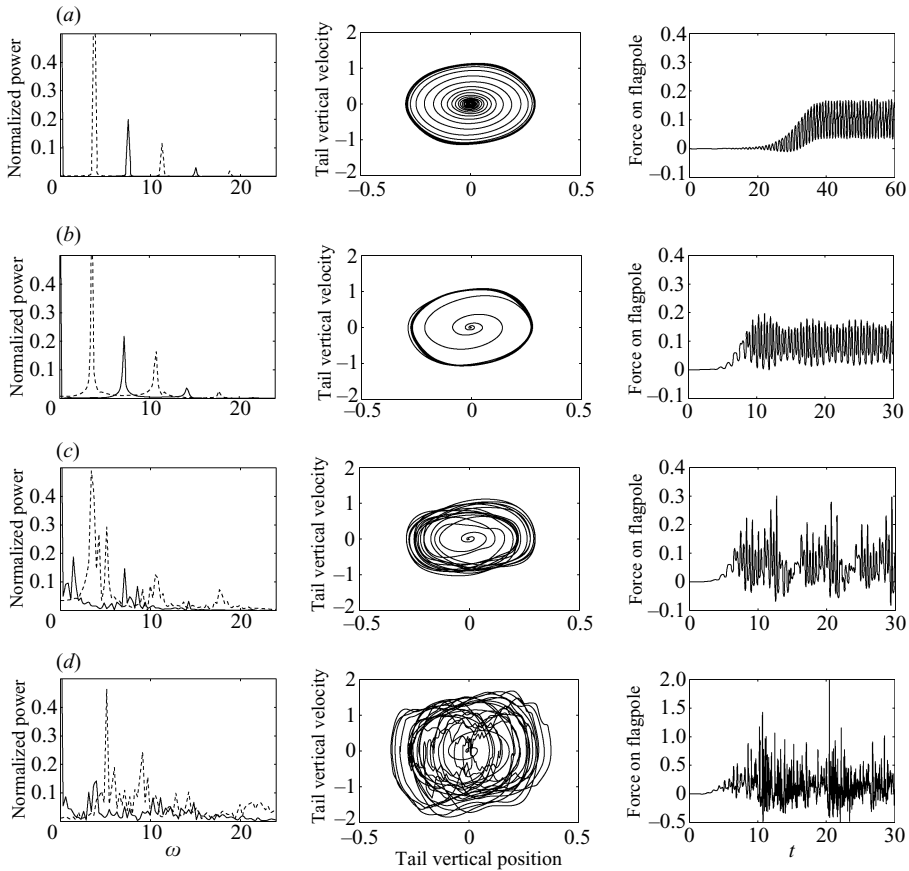
FIGURE 3. Left: frequency spectrum of the solid energy E (solid) and of the tail orientation $\theta(1, t)$ (dashed) normalized by their maximum values for clarity. Centre: tail vertical velocity vs. tail vertical displacement phase plot. Right: time variations of the horizontal force on the flagpole. $M^* = 3$ and (a) $U^* = 10$, (b) 12, (c) 13 and (d) 15.

horizontal force applied by the flag on its attachment pole at $s = 0$ also shows this strong periodicity (right-hand column of figure 3a, b).

When the flow velocity is increased further, the periodicity breaks down. The tail trajectory in the phase diagram shows a weaker limit-cycle behaviour at $U^* = 13$ and periodicity is lost at $U^* = 15$ (see centre column of figure 3). A transition from a discrete energy spectrum (figure 3a, b) to a broadband spectrum (figure 3c, d) is observed. This strong unsteadiness, also observed for the force on the flagpole, leads to snapping events (large acceleration of the flag tail) inducing peak values of the force on the flagpole of up to ten times its mean value in the flapping regime (see right-hand column of figure 3d).

3.2. *Comparison with linear stability results*

For a given M^*, the critical velocity U_c^* above which the rest state of the flag becomes unstable is computed. The corresponding critical curve is plotted in figure 4 in both the (M^*, U^*) and (μ, η) planes for comparison with previous studies. We also plot for reference the results from the linear stability analysis (Kornecki *et al.* 1976), which have been presented and confirmed experimentally in Eloy *et al.* (2008).
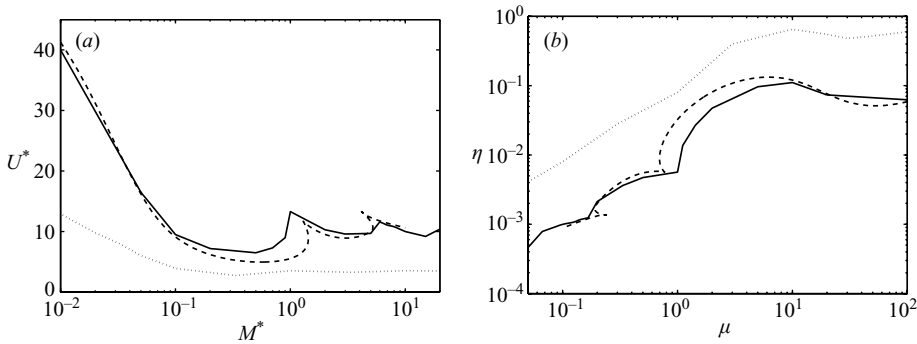
FIGURE 4. Critical curve for the stability of the flag state of rest using the present point vortex model (solid) and linear stability analysis presented in Eloy *et al.* (2008) following the method of Kornecki *et al.* (1976) (dashed). The same critical curve obtained using the vortex sheet approach (Alben & Shelley 2008) is plotted (dotted) for comparison. (a) (M^*, U^*) space, (b) (μ, η) space.
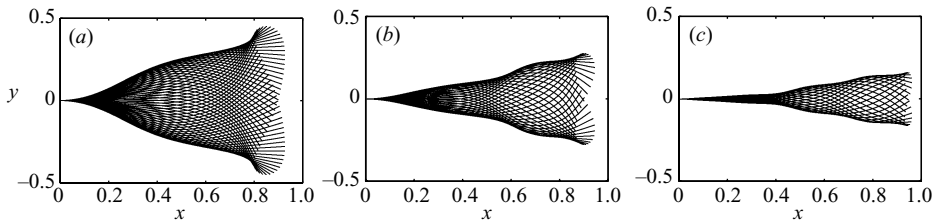

FIGURE 5. Flapping mode observed for different values of the inertia ratio: (a) $M^* = 0.5$, $U^* = 9$; (b) $M^* = 3$, $U^* = 12$; (c) $M^* = 10$, $U^* = 12$. The position of the flag is plotted every $\Delta t = 0.04$.

We observe that the present point vortex method matches very well the stability region predicted by the linear analysis, particularly the existence of several branches corresponding to different mode structures, and does significantly better than the vortex sheet model which underpredicts the critical velocity U_c^*.

3.3. *Flapping modes*

As experimentally observed by Eloy *et al.* (2008) and predicted by the linear stability analysis, each branch of figure 4 corresponds to a different mode structure: the first branch ($M^* < 1$) corresponds to mode 2 (one neck), while the second ($1 < M^* < 7$) and third ($8 < M^*$) correspond respectively to mode 3 (two necks) and mode 4 (three necks). This mode structure is observed in the large-amplitude flapping results of our model (see figure 5). The flapping mode structure seems to be determined by the most linearly unstable mode. Several other forms of initial perturbations have been tested to try to trigger a different mode (in particular transient periodic forcing at the desired frequency) without any change in the resulting dominant mode structure in the permanent regime.

3.4. *Hysteresis behaviour*

Experimental studies on flapping flags have pointed out the hysteresis behaviour of the flag when the velocity of the flow at infinity is varied (Zhang *et al.* 2000; Shelley *et al.* 2005; Eloy *et al.* 2008). Starting from rest, the flag remains straight until the critical velocity U_{c1}^* is reached, at which point a periodic flapping of large amplitude
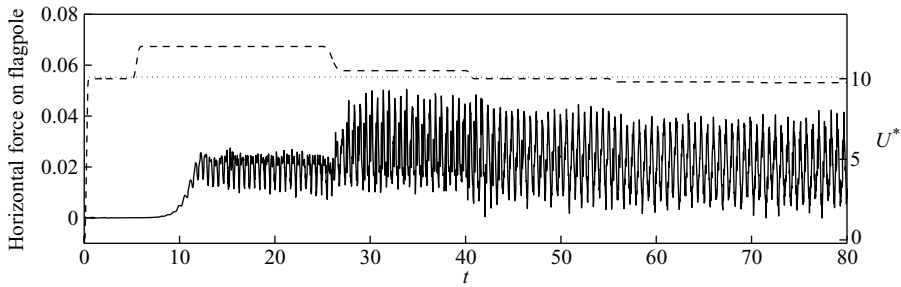
FIGURE 6. Hysteresis behaviour at $M^* = 10$: horizontal force on the flagpole (solid) and horizontal velocity of imposed flow (dashed). The critical velocity $U_{c1}^* = 10.1$ is plotted for reference (dotted). Initially, when $U^* < U_{c1}^*$ the initial perturbation is damped exponentially. Flapping develops when U^* is increased above the critical value. When U^* is then gradually reduced, it is possible to maintain a flapping state until $U^* = U_{c2}^* = 9.6 < U_{c1}^*$. If U^* is further decreased, the flapping amplitude decreases exponentially (not shown).

develops. However, if the flow velocity is subsequently reduced, large scale flapping is maintained until $U^* = U_{c2}^*$, with $U_{c2}^* < U_{c1}^*$.

Such behaviour is observed here (figure 6). The width of the hysteresis cycle ($\sim 4.5\%$) is comparable to that observed in Alben & Shelley (2008), but much smaller than that observed in the experiments ($\sim 20\%$ for Eloy *et al.* 2008). Alben & Shelley (2008) suggested that dissipative effects of viscosity or structural damping can be at the origin of these discrepancies.

3.5. *Travelling waves along the flapping flag*

This section focuses on the flapping regime that develops at intermediate velocity U^* and studies the propagation of waves along the flag in that regime. Empirical orthogonal functions (EOFs) (also known as proper orthogonal decomposition) are used to decompose a signal $f(s,t)$ into a superposition of normal modes $f(s,t) = \sum a_n(t)b_n(s)$. The modes' spatial and temporal structures are such that, when truncated at any order, the root mean square of the residue is minimized (Wallace & Dickinson 1972). The complex empirical orthogonal function (CEOF) decomposition is well-suited to identify moving patterns. The EOF decomposition is applied to the complex function $F = f + \mathrm{i} f^H$ where f^H is the Hilbert transform of f (see Barnett 1983, for more details). We have

$$f(s,t) = \mathrm{Re}\left[\sum_n A_n(t)\bar{B}_n(s) \right] = \sum_n a_n(t)b_n(s)\cos(\psi_n(t) - \phi_n(s)) \qquad (3.1)$$

where $A_n = a_n \mathrm{e}^{\mathrm{i}\psi_n}$ and $B_n = b_n \mathrm{e}^{\mathrm{i}\phi_n}$ can be obtained from the singular value decomposition of the discrete representation of F. The advantage of this method becomes apparent when this decomposition is applied to the flag problem: for example, for $M^* = 10$ and $U^* = 11$, θ can be represented by its first CEOF with a root-mean-square error of less than 1%. The spatial amplitude b gives the shape of the mode considered, and the temporal amplitude a gives the temporal fluctuations of the mode amplitude. In the highly periodic regimes considered here, a is very close to a constant.

We are most interested in the phase functions ψ and ϕ whose variations are shown in figure 7 for the first mode of the orientation, pressure force and normal elastic force in the periodic flapping regime. The temporal phase ψ is a linear function with a slope equal to the fundamental frequency ω_0 of the mode and the spatial phase
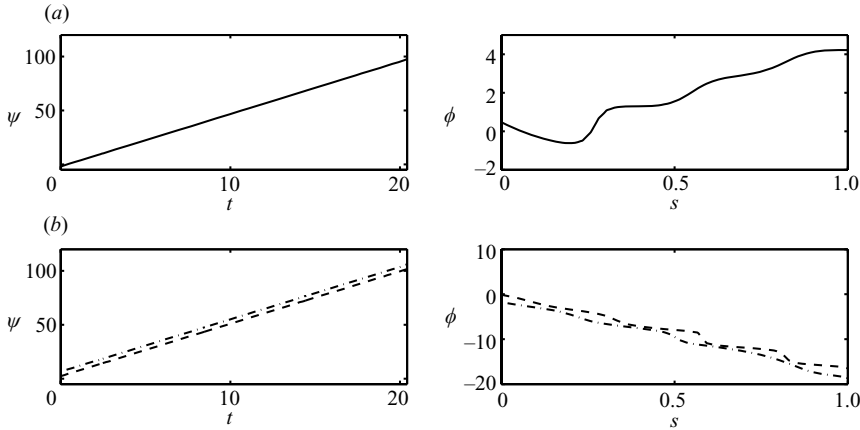
FIGURE 7. Temporal (left) and spatial (right) variations of the phase of the first CEOF in the flapping regime at $M^* = 10$ and $U^* = 11$, for (a) the orientation of the flag $\theta(s, t)$ and (b) the local pressure force (dash-dotted) and the normal component of the elastic forces in the flag (dashed). The range of t used covers about 16 periods of the flapping regime. $\dot{\psi} > 0$, therefore monotonic variations of ϕ and $\phi_s > 0$ (resp. $\phi_s < 0$) indicate a wave travelling to the right (resp. left).

ϕ has a linear trend away from the clamped corner, suggesting the propagation of waves along the flag. A phase speed in s can be defined from (3.1) as $c^{(s)} = \dot{\psi}/\phi_s$. Because of the flag deformation, $c^{(x)}$, the wave speed in x, is of the same sign and $|c^{(x)}| < |c^{(s)}|$.

For the orientation angle θ, $c^{(s)} > 0$ and the corresponding $c^{(x)}$ is close to U_∞: the deformation wave is created and advected by the outside flow. We refer to this wave as the *direct kinematic wave*, as all the kinematic fields (orientation, position and velocity) follow the same pattern. A horizontal wave speed not greater than U_∞ in this passive drag-producing configuration is consistent with the work of Lighthill (1960), where thrust production is associated with deformation waves travelling faster than U_∞.

However, we observe that the pressure and normal elastic forces in the flag have the form of a wave travelling upstream from the trailing edge where vorticity shedding prescribes the pressure jump as (2.7) simplifies at the trailing edge to $[p]^\pm = -\dot{\Gamma}_N$ (figure 7). This pressure disturbance is carried upstream along the flag by its elastic rigidity. Note that this *reverse dynamic wave* travels slower than the direct kinematic wave propagates downstream. A similar behaviour was observed for the tension in the flag.

4. Conclusions

We have shown that the unsteady point vortex model is able to reproduce both qualitatively and quantitatively the physical characteristics of the flapping of a flexible flag. The use of point vortices rather than full vortex sheets removes several computational issues due to the kernel singularities in the advection of free vortex sheets, and significantly reduces the computational complexity and cost.

The stability of the flag's state of rest and the structure of the flapping modes were studied and found to be in very good agreement with the analysis of Kornecki *et al.* (1976), which has been compared by Eloy *et al.* (2008) to experimental results. An analysis of the flapping regime showed the existence of direct kinematic waves (orientation, position and velocity) travelling with the same direction and velocity as the imposed flow, and the existence of reversed dynamic waves (pressure jump

and elastic force) travelling in the opposite direction and carrying upstream from the trailing edge the pressure change induced by the vortex shedding. The dynamics of these waves, including the influence of M^* and U^*, will be explored further in follow-on work. The present model can be extended to study flapping structures tethered to massive substrates (e.g. botanical applications). Future work will also include the study of two parallel flags as described in Zhang *et al.* (2000) to understand the coupling between the two flags and its influence on the stability and mode structure.

REFERENCES

ALBEN, S. & SHELLEY, M. J. 2008 Flapping states of a flag in an inviscid fluid: bistability and the transition to chaos. *Phys. Rev. Lett.* **100**, 074301.

BALINT, T. S. & LUCEY, A. D. 2005 Instability of a cantilevered flexible plate in viscous channel flow. *J. Fluids Struct.* **20**, 893–912.

BARNETT, T. P. 1983 Interaction of the Monsoon and Pacific trade wind system at interannual time scales. Part I: The equatorial zone. *Mon. Weath. Rev.* **111**, 756–773.

BROWN, C. E. & MICHAEL, W. H. 1954 Effect of leading edge separation on the lift of a delta wing. *J. Aero. Sci.* **21**, 690–694 & 706.

CONNELL, B. S. H. & YUE, D. K. P. 2007 Flapping dynamics of a flag in uniform stream. *J. Fluid Mech.* **581**, 33–67.

CORTELEZZI, L. 1996 Nonlinear feedback control of the wake past a plate with a suction point on the downstream wall. *J. Fluid Mech.* **327**, 303–324.

CORTELEZZI, L. & LEONARD, A. 1993 Point vortex model of the unsteady separated flow past a semi-infinite plate with transverse motion. *Fluid Dyn. Res.* **11**, 263–295.

ELOY, C., LAGRANGE, R., SOUILLIEZ, C. & SCHOUVEILER, L. 2008 Aeroelastic instability of a flexible plate in a uniform flow. *J. Fluid Mech.* **611**, 97–106.

ELOY, C., SOUILLIEZ, C. & SCHOUVEILER, L. 2007 Flutter of a rectangular plate. *J. Fluids Struct.* **23**, 904–919.

HUANG, L. 1995 Flutter of cantilevered plates in axial flow. *J. Fluids Struct.* **9**, 127–147.

JONES, M. A. 2003 The separated flow of an inviscid fluid around a moving plate. *J. Fluid Mech.* **496**, 405–441.

KORNECKI, A., DOWELL, E. H. & O'BRIEN, J. 1976 On the aeroelastic instability of two-dimensional panels in uniform incompressible flow. *J. Sound Vib.* **47**, 163–178.

LIGHTHILL, M. J. 1960 Note on the swimming of slender fish. *J. Fluid Mech.* **9**, 305–317.

MICHELIN, S. & LLEWELLYN SMITH, S. G. 2008 An unsteady point vortex method for coupled fluid-solid problems. (submitted). *Theor. Comp. Fluid. Dyn.*

RAYLEIGH, LORD 1878 On the instablity of jets. *Proc. Lond. Math. Soc.* **10**, 4–13.

ROTT, N. 1956 Diffraction of a weak shock with vortex generation. *J. Fluid Mech.* **1**, 111–128.

SAFFMAN, P. G. 1992 *Vortex Dynamics*. Cambridge University Press.

SHELLEY, M., VANDENBERGHE, N. & ZHANG, J. 2005 Heavy flags undergo spontaneous oscillations in flowing water. *Phys. Rev. Lett.* **94**, 094302.

SHUKLA, R. K. & ELDREDGE, J. D. 2007 An inviscid model for vortex shedding from a deforming body. *Theor. Comput. Fluid Dyn.* **21**, 343–368.

WALLACE, J. M. & DICKINSON, R. E. 1972 Empirical orthogonal representation of time series in the frequency domain. Part I: Theoretical considerations. *J. Appl. Met.* **11**, 887–892.

WATANABE, Y., SUZUKI, S., SUGIHARA, M. & SUEOKA, Y. 2002 An experimental study of paper flutter. *J. Fluids Struct.* **16**, 529–542.

ZHANG, J., CHILDRESS, S., LIBCHABER, A. & SHELLEY, M. 2000 Flexible filaments in a flowing soap film as a model for one-dimensional flags in a two-dimensional wind. *Nature* **408**, 835–839.

ZHU, L. & PESKIN, C. 2002 Simulation of flapping flexible filament in a flowing soap film by the immersed boundary method. *J. Comput. Phys.* **179**, 452–468.